Journal of Power Sources 446 (2020) 227312

Contents lists available at ScienceDirect

Journal of Power Sources

journal homepage: www.elsevier.com/locate/jpowsour

Temperature-dependent gas accumulation in polymer electrolyte membrane electrolyzer porous transport layers

CH. Lee [a], J.K. Lee [a], B. Zhao [a,b], K.F. Fahy [a], J.M. LaManna [c], E. Baltic [c], D.S. Hussey [c], D. L. Jacobson [c], V.P. Schulz [d], A. Bazylak [a,*]

[a] Thermofluids for Energy and Advanced Materials (TEAM) Laboratory, Department of Mechanical and Industrial Engineering, University of Toronto Institute for Sustainable Energy, Faculty of Applied Science and Engineering, University of Toronto, Toronto, Ontario, M5S 3G8, Canada
[b] Department of Civil Engineering, McMaster University, Hamilton, Ontario, L8S 4L7, Canada
[c] Physical Measurement Laboratory, National Institute of Standards and Technology, Gaithersburg, MD, USA
[d] Department of Mechanical Engineering, Cooperative State University Mannheim, Coblitzallee 1-9, 68163, Mannheim, Germany

HIGHLIGHTS

- Increasing the temperature leads to decreased gas volume in the PTL.
- Increasing the temperature leads to uniform gas volume in the PTL.
- Increasing the temperature leads to decreased dissolved oxygen in the PTL.
- Increasing the temperature leads to decreased mass transport overpotential.

GRAPHICAL ABSTRACT

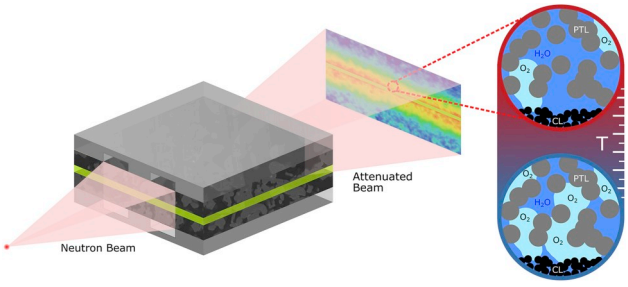

ARTICLE INFO

Keywords:
Two-phase flow
Porous transport layer
Operating temperature
Polymer electrolyte membrane electrolysis
Neutron imaging
Computational fluid dynamics

ABSTRACT

We investigate the temperature-dependent gas saturation in the porous transport layer (PTL), and the subsequent impact of this gas saturation on the mass transport overpotential of a polymer electrolyte membrane (PEM) electrolyzer. Via *in operando* neutron imaging of a PEM electrolyzer, we observe that increasing the operating temperature results in a) the reduction of gas saturation in the PTL (particularly near the catalyst layer (CL)-PTL interface) and b) the promotion of uniform gas distributions near the CL-PTL interface. Via two-dimensional computational fluid dynamics modelling of the PEM electrolyzer, we observe that increasing the operating temperature results in a) the reduction of dissolved oxygen concentrations and b) the promotion of uniform dissolved oxygen concentrations near the CL-PTL interface. Therefore, we attribute our observation of lower and more uniform gas saturation to correspondingly lower and more uniform gas evolution rates that would accompany the dissolved oxygen concentrations predicted by our model. Increasing the operating temperature leads to lower mass transport overpotentials, which we attribute to the combined effects of lower and more uniform gas saturations and lower dissolved oxygen concentrations near the CL-PTL interface. Based on this work, we recommend higher operating temperatures for optimal water and oxygen transport in the PTL.

* Corresponding author. Mechanical & Industrial Engineering, Faculty of Applied Science & Engineering, University of Toronto, 5 King's College Road, Toronto, ON, M5S 3G8, Canada.
E-mail address: abazylak@mie.utoronto.ca (A. Bazylak).

https://doi.org/10.1016/j.jpowsour.2019.227312
Received 2 August 2019; Received in revised form 12 September 2019; Accepted 14 October 2019
Available online 26 November 2019
0378-7753/

1. Introduction

Over the last few decades, the climate has warmed at an unprecedented rate, largely due to human-induced changes to the atmosphere [1]. Specifically, the global emission of carbon dioxide is anticipated to triple from 1975 to 2020, highlighting the urgent need for a zero-carbon-emission energy infrastructure [2]. Despite significant research and developments in sustainable energy technologies, such as wind and solar, the integration of sustainable energy sources to the electrical grid remains challenging due to the intermittent nature of such energy sources [3]. The polymer electrolyte membrane (PEM) electrolyzer offers a promising solution by providing a means to store intermittent energy in the form of hydrogen gas. For the widespread adoption of this technology, the efficiency of PEM electrolyzers must be improved [4].

Although commercial PEM electrolyzers operate at $T = 60\,^{\circ}C$ [5], higher temperature operation is a key area for future PEM electrolyzer research [5] due to the favorable impact of increasing temperature on electrolyzer efficiency [4–9]. Specifically, higher temperature operation has been shown to reduce the kinetic overpotential, ohmic overpotential, and reversible potential [8]. Although the impact of temperature on the kinetic and ohmic overpotentials has been extensively studied [4–11], further investigations are critical for motivating higher temperature operation, such as the effects of temperature on degradation [12] and mass transport overpotentials [8]. In particular, understanding the temperature-dependence of mass transport losses is a necessary first step to advancing commercial-scale PEM electrolyzers for higher temperature operation.

Mass transport-related issues are a main source of inefficiency in a PEM electrolyzer. Gaseous oxygen, a by-product of the anode reaction, accumulates in the anode porous transport layer (PTL) and impedes the reactant (liquid water) from reaching the reaction sites. Specifically, under typical industrial operating conditions (i.e. current density ranging from 1 A/cm^2 to 5 A/cm^2 and operating pressure of 1 bar–100 bar), the mass transport overpotential contributes up to 25 % of the total overpotential of PEM electrolysis [13]. Additionally, mass transport overpotential increases exponentially with increasing current density under water starvation conditions [14], which leads to cell failure and severe component damage [15]. Although extensive research efforts have been made to understand gas and liquid transport through the anode PTL [16–32], the change in temperature adds complexity to characterizing the gas evolution in the PTL, since relevant fluid and transport properties (including viscosity, density, surface tension, solubility, and diffusivity) are highly temperature-sensitive.

The ubiquitous relationship between temperature and fluid flow in permeable media is important in many applications such as bioremediation [33], and enhanced oil recovery [34]; however, the effect of temperature in gas-evolving porous electrodes has been given much less emphasis. Recent works [8,35] reported opposing correlations between the operating temperature and the mass transport overpotential in PEM electrolyzers. Specifically, Suermann et al. [8] observed a decrease in mass transport overpotential with increasing temperature, which they attributed to favorable changes in water viscosity and surface tension. Ojong et al. [35] showed, via semi-empirical modelling, that mass transport overpotentials increased with increasing temperature, which they attributed to increased gas coverage at the reaction sites. Furthermore, Li et al. [36] demonstrated, via optical imaging, that slug formation at higher temperatures in the anode flow channels enhance bubble removal from the reaction sites. These existing works [8,35,36] illustrate the complex relationship between the operating temperature and the two-phase flow behavior through the PTL. Suermann et al. [8] highlighted the need for an *in operando* imaging approach to understand the impact of temperature on the two-phase flow behavior in the PTL, especially near the anode catalyst layer-PTL interface (hereafter termed CL-PTL interface). Neutron imaging is particularly beneficial for imaging micrometer-scale gas bubbles in metallic porous materials due to the high sensitivity of neutrons to water and low sensitivity to metals [21, 37-39]. Selamet et al. [40] observed through neutron imaging that the gas saturation in mesh-type PTLs increased with increasing temperature. *In operando* imaging with neutrons presents a valuable opportunity to understand the temperature-dependent transport of oxygen in the PTL, particularly near the CL-PTL interface.

In this work, we explored the impact of temperature on oxygen transport in the PTL (particularly near the CL-PTL interface) of PEM electrolyzers via neutron imaging coupled with 2D computational fluid dynamics modelling. Herein, we report the benefits of increasing the operating temperature for improved mass transport, which leads to lower and more uniform gas saturation and reduced dissolved oxygen concentration near the CL-PTL interface.

2. Methodology

In this section, we describe the electrolyzer hardware used to characterize multiphase transport phenomena in the PEM electrolyzer (section 2.1). We next describe our *in operando* neutron imaging apparatus, experimental procedures, and the image processing steps (section 2.2). We present our two-dimensional computational fluid dynamics (2D CFD) model that was used to interpret our neutron imaging results (section 2.3). Finally, we detail our electrochemical analyses procedure (section 2.4).

2.1. Electrolyzer components and operation protocol

We designed a custom PEM electrolyzer for *in operando* in-plane neutron imaging (beam parallel to the active area). The electrolyzer cell featured titanium flow fields with 16 parallel channels separated by 0.5 mm wide lands, and the height and width of the channels were 0.5 mm and 0.5 mm, respectively. Titanium flow fields with parallel flow channels were employed for both the anode and the cathode compartments to replicate the conditions of a PEM electrolyzer used in industry [41,42]. The flow field was plated with 0.5 μm thick gold and 2.5 μm thick platinum to avoid the formation of oxide layers on the titanium surface. Sintered titanium powder sheet PTLs with a porosity of 35 % and a thickness of 250 μm (1100 series,[1] Mott Corp.) were used on the anode and cathode. Both PTLs were compressed to 240 μm with rigid polytetrafluoroethylene (PTFE) gaskets. A commercial catalyst coated Nafion HP membrane (HYDRion HP, Ion Power) was used. The cathode platinum areal density was 0.3 mg/cm^2, and the anode iridium areal density was 1.0 mg/cm^2. The active area was 5 mm long (along the direction traversed by the neutron beam) and 16 mm wide.

Pre-heated deionized water was supplied to both the anode and the cathode compartments at 20 mL/min using a peristaltic pump (Masterflex L/S precision variable-speed console drive, Cole-Parmer). A large water stoichiometry (up to 137) was employed to replicate the conditions of an industrially operating PEM electrolyzer [41]. The supplied water was pre-heated using an in-line heater (Watlow fluent inline heater 500 W, Zesta Engineering LTD.), and the temperature was controlled using a proportional integral derivative (PID) temperature controller (Zesta benchtop PID control & limit, Zesta Engineering LTD.) and an in-line thermocouple. We applied direct current to the cell through a power supply (Genesys 750 W, TDK-Lambda). The electrolyzer was tested over a range of current densities (i): 0.5 A/cm^2, 1.0 A/cm^2, 1.5 A/cm^2, 2.0 A/cm^2, 2.5 A/cm^2, and 3.0 A/cm^2. At each current density, a 20 min hold

[1] Certain trade names and company products are mentioned in the text or identified in an illustration in order to adequately specify the experimental procedure and equipment used. In no case does such identification imply recommendation or endorsement by the National Institute of Standards and Technology, nor does it imply that the products are necessarily the best available for the purpose.

was performed to achieve steady state operation. The electrolyzer was operated galvanostatically to ensure that the number of oxygen molecules produced is identical regardless of the operating temperature.

The experiment was conducted at the following operating temperatures: 40 °C, 60 °C and 80 °C. The temperatures were kept below the boiling temperature (i.e. T = 100 °C) at atmospheric pressure to avoid water vapor formation due to boiling. For temperature control, a water circulation bath (Isotemp heated bath circulator, Fisher Scientific) was used to circulate pre-heated water through the end plates of the cell. We flushed the electrolyzer cell with liquid water for 20 min before switching to the temperature set point, ensuring the complete removal of any residual gas from the PTL.

2.2. Neutron imaging and processing

In operando neutron imaging was performed at the Neutron Imaging Facility (BT-2) at the National Institute of Standards and Technology (NIST) in Gaithersburg, Maryland [43]. The electrolyzer cell was oriented in the in-plane direction of the neutron beam (i.e., membrane parallel to the beam axis). Through-plane imaging (membrane perpendicular to the beam axis) is typically used to quantify the gas distribution in the anode flow channels [44]. Here, we used an in-plane imaging configuration (membrane parallel to the beam axis) to resolve the gas saturation distribution near the CL-PTL interface. After transmitting through the cell, the neutron beam was absorbed by the scintillator (Gd_2O_2S:Tb), which emits visible light upon absorbing neutron particles. This visible light was captured by a scientific complementary metal-oxide semiconductor (Andor Neo sCMOS, Oxford Instruments) sensor. The exposure time was 25 s, the pixel pitch was 6.5 μm, and the spatial resolution was ~20 μm. Two types of images were captured: reference images (Fig. 1a) when the PTLs were fully saturated with liquid water and the cell was not operating (*i.e.*, $i = 0$ A/cm^2), and operational images (Fig. 1b) when the cell was operating (*i.e.*, $i > 0$ A/cm^2).

Each reference and operational image underwent an image processing procedure to minimize the effect of inherent artefacts stemming from the experimental setup. Three types of artefacts were removed: (1) gamma spots, (2) hot spots, and (3) beam intensity dynamics. The gamma spots originated from high-energy photons generated as a by-product of neutron imaging and manifested as spatially inconsistent noise. The gamma spots were eliminated through the median-combination filtering of three sequential images. Hot spots originated from the hardware (such as the detector) and manifested as spatially consistent noise. The hot spots were eliminated through two-dimensional median-filtering over a 3 pixel by 3 pixel area. Finally, a shift in the intensity profile occurred during imaging due to the fluctuation of the beam source at the BT-2 beamline [45]. An image registration process developed by Hussey et al. [43] was used to correct the movement in the intensity profile in the images.

We used the processed reference and operational images to quantify the gas thickness in the PTL (Fig. 1c). We applied the calibrated Beer-Lambert law reported by Hussey et al. [43], as follows:

$$t_{gas} = \sqrt{-\frac{\ln(I/I_0)}{\beta_w} + \frac{\Sigma_w^2}{4\beta_w^2}} - \frac{\Sigma_w}{2\beta_w}, \quad (1)$$

where t_{gas} is cumulative thickness of the gas phase along the direction traversed by the neutron beam [mm], I is the pixel intensity from the operational images, and I_0 is the pixel intensity from the reference image. In Equation (1), β_w [-0.00947 mm^{-2}] and Σ_w [0.38483 mm^{-1}] are non-linear least square fitting parameters [44]. The gas saturation was calculated as the fraction of gas volume to the total pore volume as follows:

$$S = \frac{t_{gas}}{L_{PTL} \cdot \varphi}, \quad (2)$$

where t_{gas} is the cumulative gas thickness, L_{PTL} is the length of the PTL in the neutron beam path [5 mm], and φ is the porosity of the PTL [φ

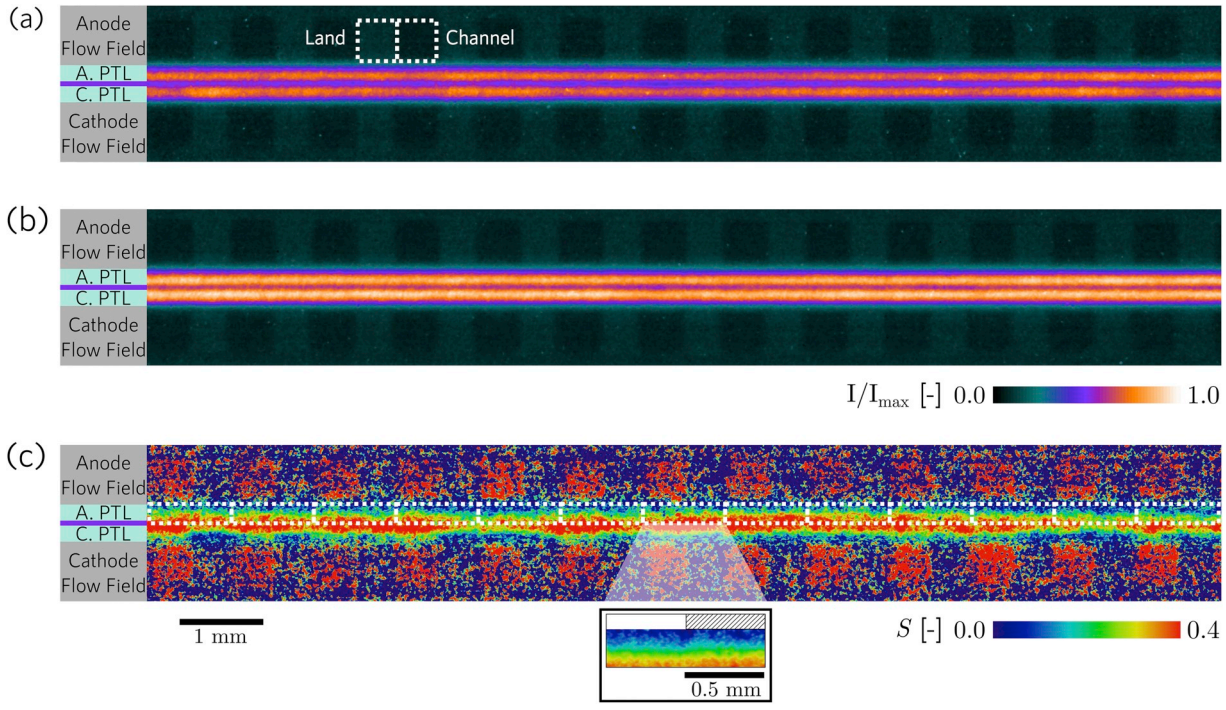

Fig. 1. Image processing procedure for quantifying gas distribution in the PTL in an operating electrolyzer. Processed radiographs of the PEM electrolyzer (a) before and (b) during operation. The white-dashed square boxes indicate the land and the channel in the anode flow field. (c) The Beer-Lambert law was applied to obtain the fraction of gas volume in the PTL. The anode PTL regions underneath the lands and channels were paired, and an average of 13 pairs (white-dashed rectangular boxes in (c)) were examined.

= 0.35]. We assumed that the compression had a negligible effect on the resulting PTL porosity, since titanium-based PTLs have poor compressibility [46]. The porosity of the PTL was obtained via micro-computed tomography of an uncompressed PTL used in this study. For each current density, one representative operational image was obtained by averaging the images that corresponded to the last 5 min of the operation. Lastly, the gas phase distributions for the channel and land regions were obtained by averaging over the 13 pairs of channel and land regions of the PTL (Fig. 1c). We assumed the anode PTL region extended from the anode flow field/PTL interface to a thickness of 240 μm towards the membrane, since the 240 μm thick PTFE gaskets were used to ensure that the PTL thickness was ≥ 240 μm. For illustrative purposes in Fig. 1c, a white box is positioned above the channel region, and a hashed box is positioned above the land region.

2.3. 2D computational fluid dynamics

We used computational fluid dynamics (CFD) to elucidate the mechanistic cause of increased oxygen gas accumulation in the PTL with increasing temperature. In this work, a single-phase CFD tool was developed to simulate the dissolved oxygen concentration in the liquid water phase within the PTL. The ratio between the dissolved oxygen concentration and the solubility is termed thermodynamic supersaturation and is an indicator used to describe the rate of gas nucleation on gas-evolving electrodes [47,48]. Specifically, the higher the thermodynamic supersaturation, the higher the rate of gas nucleation on an electrode surface. It has been experimentally observed that the thermodynamic supersaturation needs to be approximately 310 for hydrogen bubbles to nucleate on a platinum electrode [49]. This thermodynamic supersaturation was used to measure the dependence of the gaseous oxygen generation rate within the PTL on the operating temperature.

In this section, we describe the domain that was used for the computational fluid dynamics simulation (section 2.3.1). We state and justify each assumption that was used in this simulation (section 2.3.2). We also detail the equations, detailed derivations, and numerical approach for solving the equations (section 2.3.3).

2.3.1. Domain

The domain used in this simulation corresponds to a single channel and land region pair (Fig. 2). $H = 0.24$ mm is the thickness of the PTL and the domain length in the *y*-direction, and $w_{total} = 1$ mm is the width of a single land and channel pair and the domain length in the x-direction. A grid density of 37-by-154 was employed after performing a grid sensitivity study (based on < 3 % change in bulk O_2 concentration), and the width and height of each grid was 6.5 μm (selected to match the pixel size of the neutron images).

We set the boundary conditions to represent an operating electrolyzer as follows:

PTL-Channel Interface:

$$C_{O_2}\left(0 \le x \le w_{total}/2, y = H\right) = 0 \tag{3}$$

PTL-Land Interface:

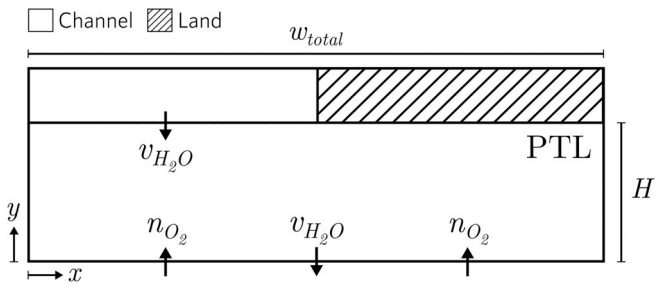

Fig. 2. Computational domain showing the boundary conditions.

$$\frac{\delta C_{O_2}}{\delta y}\left(\frac{w_{total}}{2} + 1 \le x \le w_{total}, y = H\right) = 0 \tag{4}$$

CL-PTL Interface:

$$\frac{\delta C_{O_2}}{\delta y}(y = 0) = n_{O_2} \Big/ D^{i,j}_{O_2,eff} \tag{5}$$

where C_{O_2} is the concentration of oxygen in liquid water [mol/m^3] and $D^{i,j}_{O_2,eff}$ is the effective diffusivity of oxygen in liquid water when the PTL is partially-gas-saturated at [m^2/s]. n_{O_2} is given by Faraday's law:

$$\dot{n}_{O_2} = \frac{I}{zF} \tag{6}$$

where I is the current, z is the number of electrons transferred per oxygen (4 e$^-$), and F is Faraday's constant (96485 C/mol).

2.3.2. Assumptions

We detail the numerical modelling assumptions and the associated justifications below:

(1) *Steady-state.* Since we obtained *in operando* neutron images under steady-state conditions (images were taken during the last 10 min of operation), we assumed that the oxygen concentration profile was also steady-state.

(2) *The system was assumed to be isothermal.* Liquid water that was preheated to the desired temperature was supplied to the anode flow channels with a high flow rate during the experiment (water stoichiometry up to 137). The cell was also actively heated/cooled using a circulating water bath that supplied liquid water to the cooling channels in the end plates. Therefore, we assumed an isothermal system for the simulation.

(3) *The velocity of liquid water (v_{H_2O}) entering the PTL via the channel was equal to the velocity of consumed liquid water.* The velocity of consumed liquid water was defined as the volumetric water flow rate consumed due to the reaction, divided by the active area of the cell. From mass conservation, liquid water entering the PTL was also consumed at the catalyst layer. Channel-to-channel convection was assumed to be negligible since parallel flow channels were used in this study.

(4) *The gaseous phase was assumed to be impermeable.* In this simulation, we used gas saturation measurements obtained from neutron imaging. The gaseous phase was assumed to be a physical barrier for dissolved oxygen transport, which was taken into account when simulating the convective and diffusive transport of oxygen in liquid water. The gaseous phase was assumed to be impermeable, and phase change was not explicitly simulated. Although phase change was not simulated, oxygen solubility was used to measure the dependence of the gaseous oxygen generation rate on temperature. We assumed that the main impact of gas bubbles was in presenting a barrier to oxygen transport in the liquid phase.

(5) *The effective diffusivity of oxygen and gas saturation relationship followed a power law.* Previous works [50,51] demonstrated that for thin porous media structurally similar to PTLs (i.e. thickness, porosity, and pore size), effective diffusivity can be expressed by a power law based on the bulk diffusivity and saturation with a power of $\beta \approx 3$.

(6) *The oxygen concentration at the interface between the channel and PTL was assumed to be perfectly diluted* (i.e. $C_{O_2} = 0$). As mentioned in assumption (2), liquid water was supplied to the anode flow channel with a high flow rate during the experiment (water stoichiometry up to 137), thus we assumed that the anode flow channel experienced constant dilution. Furthermore, fresh deionized water was supplied to the electrolyzer, and the water

was not recirculated for a constant boundary condition in the anode flow channels.

(7) *A periodic boundary condition was applied to the side boundaries* ($x = 0$, $x = w_{total}$). The channel and rib pair repeated across the imaged electrolyzer cell; thus a periodic boundary condition was used to reflect this geometry.

2.3.3. Equations and numerical approach

We considered the following steady-state 2D advection-diffusion equation:

$$\nabla\left(D_{O_2,eff}\nabla C_{O_2}\right) - \nabla\cdot\left(v_{H_2O}v\cdot C_{O_2}\right) = 0 \tag{7}$$

where v_{H_2O} is the velocity of liquid water in the PTL [m/s]. This equation has been previously used to describe oxygen transport in PEM electrolyzers in previous works [35,52].

We determined the bulk diffusivity (fully-water-saturated condition in the PTL) by using a micro-computed tomography image of the PTL and solving the species conservation equation and Fick's law using an open-source pore network modelling algorithm (OpenPNM) [53]. Specifically, the micro-computed tomography image of the PTL was converted to an equivalent pore network consisting of pores and throats by using an in-house extraction algorithm [54]. Then, the equivalent pore network was imported into OpenPNM. Fick's law was used to calculate the diffusivity of oxygen in liquid water under fully-water-saturated conditions:

$$D_{O_2} = \frac{LN_{O_2}}{\left(C_{O_2,in} - C_{O_2,out}\right)} \tag{8}$$

where L is the diffusion length [m], N_{O_2} is the oxygen flux [mol/m^2/s], and $C_{O_2,in}$ and $C_{O_2,out}$ are the dissolved oxygen concentrations at the inlet and the outlet, respectively [mol/m^3]. The oxygen flux was calculated by applying the species conservation equation to each pair of neighbouring pores in the PTL:

$$N_{O_2,\mathrm{i}} = \sum_{\mathrm{j}=1}^{n} g_{\mathrm{ij}}\left(C_{O_2,\mathrm{i}} - C_{O_2,\mathrm{j}}\right) \tag{9}$$

where i and j denote the pore of interest and its neighbouring pore, respectively. $N_{O_2,\mathrm{i}}$ is the total oxygen flux at pore i, n is the total number of pores that neighbour pore i, g_{ij} is the diffusive conductance between pore i and j, and $C_{O_2,\mathrm{i}}$ and $C_{O_2,\mathrm{j}}$ are the dissolved oxygen concentrations in pore i and j, respectively. For greater details in the diffusivity calculations via pore network modelling, the readers are directed to Wong et al. [55].

We calculated the Peclet number (ratio between advective and diffusive transport rate) to determine the dominating transport mechanism in the PTL:

$$Pe = \frac{v_{H_2O}H}{D_{O_2}} \tag{10}$$

where v_{H_2O} is the liquid water velocity (4.3×10^{-7} m/s, assuming a current density of $i = 3$ A/cm^2) and H is the thickness of the PTL (250 μm). The Peclet number was small ($Pe = 1.7\times10^{-2} \ll 1$), implying that advective transport was negligible relative to diffusive transport. This simplified the advection-diffusion equation to the following:

$$\nabla\left(D_{O_2,eff}\nabla C_{O_2}\right) = 0 \tag{11}$$

We calculated $D_{O_2,eff}$ based on the gas saturation data obtained from neutron imaging, using the following correlation [50,51]:

$$D_{O_2,eff} = D_{O_2}(1-S)^{\beta} \tag{12}$$

where S is saturation [−], and $\beta \approx 3$ is an exponent parameter [50,51]. We implemented the centered-difference method for approximating the advection-diffusion equation as follows:

$$C_{O_2}^{i,j} = \left[\frac{D_{O_2,eff}^{i+\frac{1}{2},j}\cdot C_{O_2}^{i+1,j} + D_{O_2,eff}^{i-\frac{1}{2},j}\cdot C_{O_2}^{i-1,j}}{\Delta x^2} + \frac{D_{O_2,eff}^{i,j+\frac{1}{2}}\cdot C_{O_2}^{i,j+1} + D_{O_2,eff}^{i,j-\frac{1}{2}}\cdot C_{O_2}^{i,j-1}}{\Delta y^2}\right] \Bigg/ \left[\frac{D_{O_2,eff}^{i+\frac{1}{2},j} + D_{O_2,eff}^{i-\frac{1}{2},j}}{\Delta x^2} + \frac{D_{O_2,eff}^{i,j+\frac{1}{2}} + D_{O_2,eff}^{i,j-\frac{1}{2}}}{\Delta y^2}\right] \tag{13}$$

$$D_{O_2,eff}^{i+\frac{1}{2},j} = \frac{D_{O_2,eff}^{i+1,j} + D_{O_2,eff}^{i,j}}{2} \tag{14}$$

$$D_{O_2,eff}^{i-\frac{1}{2},j} = \frac{D_{O_2,eff}^{i,j} + D_{O_2,eff}^{i-1,j}}{2} \tag{15}$$

$$D_{O_2,eff}^{i,j+\frac{1}{2}} = \frac{D_{O_2,eff}^{i,j+1} + D_{O_2,eff}^{i,j}}{2} \tag{16}$$

$$D_{O_2,eff}^{i,j-\frac{1}{2}} = \frac{D_{O_2,eff}^{i,j} + D_{O_2,eff}^{i,j-1}}{2} \tag{17}$$

where i and j denote coordinates $\Delta x = \Delta y = 6.5\times10^{-6}$ m are the grid sizes in the PTL region in the x- and y-directions, respectively. We solved equations (13)–(17) via MATLAB using the Jacobi iterative method.

2.4. Electrochemical analyses

The mass transport overpotential was calculated based on the following relation [8]:

$$\eta_{\mathrm{mass\ \ transport}} = \mathrm{E_{cell}} - \mathrm{E_{reversible}} - \eta_{\mathrm{ohmic}} - \eta_{\mathrm{kinetic}} \tag{18}$$

where $\eta_{\mathrm{mass\ \ transport}}$ is the mass transport overpotential [V], $\mathrm{E_{cell}}$ is the measured cell potential [V], $\mathrm{E_{reversible}}$ is the reversible potential [V], η_{ohmic} is the ohmic overpotential [V], and η_{kinetic} is the kinetic overpotential [V]. The reversible potential was estimated using an empirical correlation reported by LeRoy et al. [56] for water electrolysis:

$$\mathrm{E_{reversible}} = 1.5184 - 1.5421\times10^{-3}\cdot\mathrm{T} + 9.523\times10^{-5}\cdot\mathrm{T}\cdot ln\mathrm{T} + 9.84\times10^{-8}\cdot\mathrm{T}^2 \tag{19}$$

where T is the operating temperature [K]. The ohmic overpotential was determined based on the current density and the measured ohmic resistance using Ohm's law:

$$\eta_{\mathrm{ohmic}} = i\cdot\mathrm{R_{ohmic}} \tag{20}$$

where i is the current density [A/cm^2], and $\mathrm{R_{ohmic}}$ is the ohmic resistance [Ω·cm^2]. In this study, $\mathrm{R_{ohmic}}$ was determined by measuring the high-frequency resistance (HFR) at 0.1 A/cm^2 at a frequency of 1 kHz and a 10 % perturbation (0.0314 Ω·cm^2, 0.0304 Ω·cm^2, and 0.0289 Ω·cm^2 for 40 °C, 60 °C, and 80 °C, respectively). The HFR was assumed to be constant across all operating current densities, since HFR is insensitive to operating current densities below 3 A/cm^2 [57].

We calculated the HFR-corrected cell potential by subtracting the ohmic overpotential from the measured cell potential. The IR-corrected cell potential shows linear behavior at low current densities, and a Tafel line can be fit to describe the kinetic overpotential as follows:

$$\eta_{\mathrm{kinetic}} = b\cdot\log_{10}\left(\frac{i}{i_0}\right) \tag{21}$$

where b is the Tafel slope [V/decade], and i_0 is the apparent exchange current density [A/cm^2]. Tafel measurements were performed using a potentiostat (VersaSTAT 3, Princeton Applied Research). In this work, the exchange current density and the Tafel slope were based on Tafel

region measurements for current densities between 30 mA/cm^2 to 100 mA/cm^2, which is consistent with the range reported in a previous work [8]. The Tafel plots used in this work are shown in Fig. A.1 (Appendix A).

We calculated $E_{reversible}$ by solving Equation (19), η_{ohmic} by solving Equation (20), and $\eta_{kinetic}$ by solving Equation (21). Lastly, we calculated the mass transport overpotential by solving Equation (18).

3. Results and discussion

We first present the *in operando* gas saturation distribution in the anode PTL with varying current densities and operating temperatures, measured via neutron imaging (section 3.1). We next estimated the dissolved oxygen concentration in the PTL via two-dimensional (2D) computational fluid dynamics (CFD) to explain the physical mechanisms behind the experimentally measured trends in gas saturation (section 3.2). Lastly, we present our electrochemical analysis to directly correlate mass transport behavior to the performance of the electrolyzer (section 3.3).

3.1. Neutron imaging: temperature-dependent gas saturation in the PTL

We present the *in operando* gas distributions in the anode PTL obtained using neutron imaging for a range of current densities ($i = 0.5$ A/cm^2 to 3.0 A/cm^2) and temperatures ($T = 40\,^\circ$C, 60 °C, and 80 °C) (Fig. 3). This series of images illustrates the inherent dependence of the PTL gas distribution on the operating temperature of the electrolyzer. We observed higher gas saturations at higher operating current densities and lower operating temperatures, particularly near the CL-PTL interface. At any given current density, the number of produced oxygen molecules is constant regardless of the operating temperature; therefore, the changes in gas saturation as a function of temperature must be driven by changes in the physicochemical characteristics of the system, such as the number of gas nucleation sites and the solubility of oxygen in water.

It is important to consider the possible effects of the operating temperature on the two-phase flow regime in the PTL, which can be characterized by the capillary number, Ca, and the viscosity ratio, M [58]:

$$\mathrm{Ca} = \frac{\mu_{H_2O} v}{\gamma} \tag{22}$$

$$\mathrm{M} = \frac{\mu_{O_2}}{\mu_{H_2O}} \tag{23}$$

where μ_{O_2} and μ_{H_2O} are viscosities of oxygen and water, respectively [Pa·s], v is the velocity of their interface [m/s], and γ is the surface tension of oxygen and water [N/m]. The viscosity ratio is very small regardless of the operating temperature ($M \ll 1$), and the possible two-phase flow regimes for $M \ll 1$ are capillary fingering and viscous fingering [58]. Capillary fingering (characterized by a low capillary number) typically results in a higher gas saturation in the PTL relative to viscous fingering (characterized by a high capillary number). A higher temperature results in a decrease in μ_{H_2O} (6.53×10^{-4} Pa·s and 3.54×10^{-4} Pa·s for $T = 40\,^\circ$C and 80 °C, respectively [59]) and γ

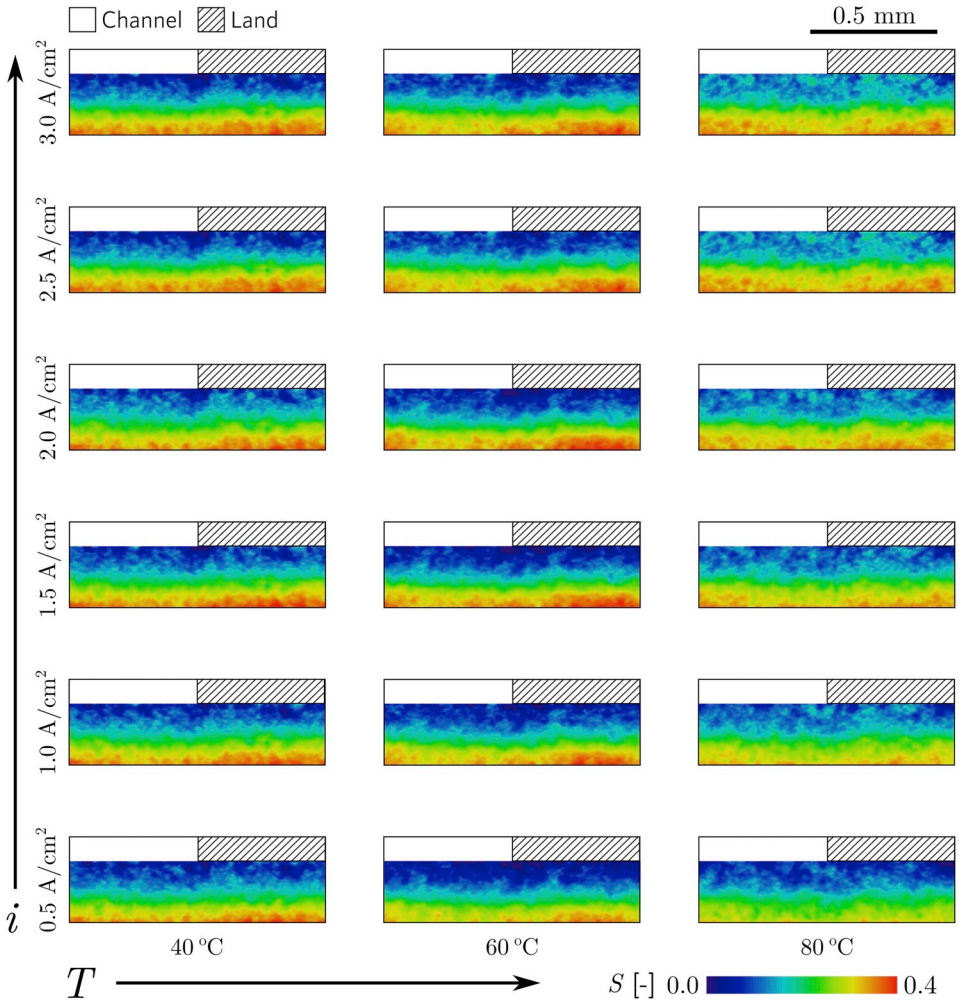

Fig. 3. Neutron images showing gas saturation distributions in the anode porous transport layers at operating current densities $i = 0.5$ A/cm^2 - 3.0 A/cm^2 and at operating temperatures $T = 40\,^\circ$C, 60 °C, 80 °C. Each image is the average of 13 pairs of channel (0.5 mm wide) and land (0.5 mm wide) regions of the PTL (see Fig. 1), and an average of images during the last 5 min of each current density operation. For illustrative purposes, a white box is positioned above the channel region, and a hashed box is positioned above the land region. Each image is an average of 5 min of steady-state operation (12 images). We observed higher gas saturations at higher current densities and lower operating temperatures.

(6.96×10^{-2} N/m and 6.27×10^{-2} N/m for T = 40 °C and 80 °C, respectively [60]). These trends in fluid properties suggest that Ca decreases with increasing temperature, and a decrease in Ca is typically accompanied by an increase in gas saturation [58]. However, our observations showed an unexpected opposite trend whereby the gas saturation decreased with increasing temperature, and the consequence of this observation is that changes to pore-scale fingering mechanisms had a negligible effect on the overall gas saturation in the PTL. Rather, we propose that a cell-scale phenomenon exists, such as a changing in the number of gas clusters within the PTL.

We quantified the average gas saturations in the region near the CL-PTL interface which we defined as the region bound by the CL-PTL interface and the plane at $y = 50$ μm (see white-dashed box in Fig. 4a) (for discussion on the region near the PTL-flow field (FF) interface, the readers are directed to Appendix B). We consistently observed the lowest gas saturation at the highest operating temperature (T = 80 °C) (Fig. 4b).

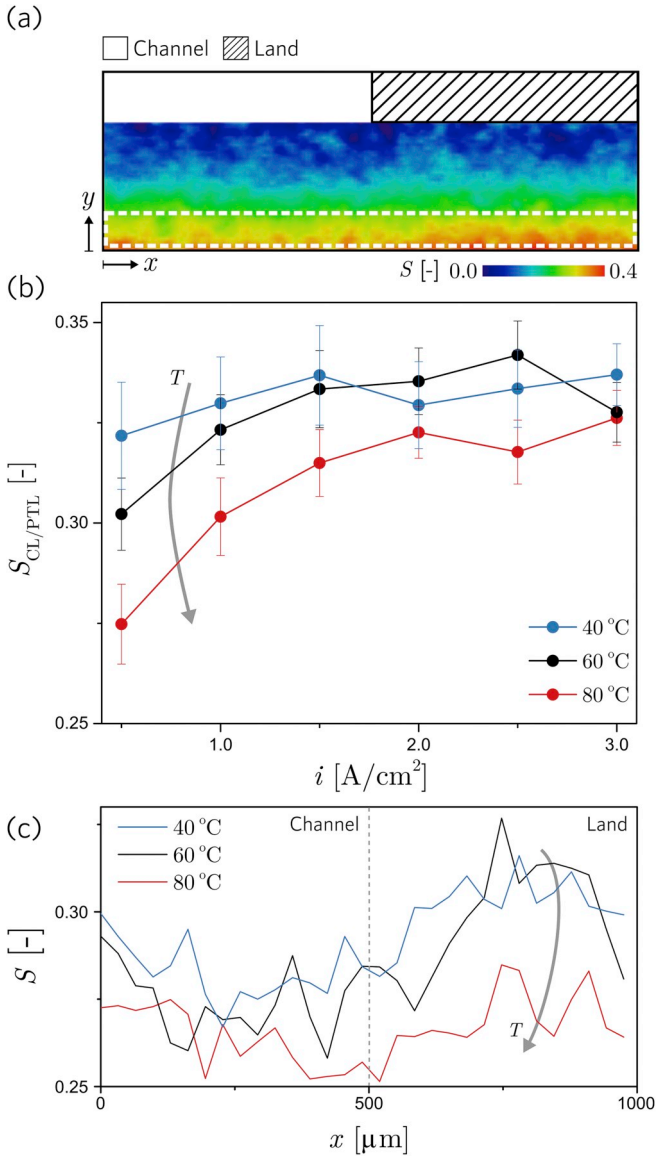

Fig. 4. Oxygen gas distributions in the anode PTL of an operating electrolyzer. (a) We quantified the average gas saturation in the region bounded by the CL-PTL interface and $y = 50$ μm (white-dashed box). (b) Average gas saturations near the CL-PTL interface. We observed the lowest gas saturation at 80 °C, particularly for $i \leq 1.5$ A/cm^2. (c) Gas saturation distribution near the CL-PTL interface in the x-direction for $i = 1$ A/cm^2. We observed that the gas saturation in the land region was higher than the channel region.

The lowest gas saturations were observed at current densities $i \leq 1.5$ A/cm^2, and at 80 °C we observed a 15 % lower gas saturation compared to 40 °C (at $i = 0.5$ A/cm^2, Fig. 4b). This distinct trend in reduced gas saturation with increasing temperature is surprising, since the solubility (saturation concentration) of oxygen in liquid water decreases with increasing temperature (57–43 mol/m^3 for 40 °C and 80 °C, respectively [61]).

Additionally, the gas distribution near the CL-PTL interface became increasingly uniform at higher operating temperatures (Fig. 4c). We quantitatively compared the gas saturation in the channel region to the land region and observed a 7 % higher gas saturation in the land region at T = 40 °C, whereas we observed a 1 % higher gas saturation in the land region at T = 80 °C. This temperature dependence in gas distribution is particularly noteworthy, since a previous work [62] attributed larger quantities of gas accumulation in the land region solely to longer gas discharge paths. In our work, while the gas discharge path is longer in the land region relative to the channel region, this distance is constant for each operating temperature. Therefore, a mass transport mechanism that has not been previously accounted for in the literature exists, and it manifests through the enhanced uniformity of gas saturation at higher operating temperatures.

3.2. CFD: temperature-dependent dissolved oxygen concentration in the PTL

We calculated the dissolved oxygen concentration in the PTL via 2D computational fluid dynamics simulations to elucidate the mechanistic cause for lower average gas saturation and more uniform gas distributions near the CL-PTL interface. Specifically, the dissolved oxygen concentration and the solubility are assumed to be key drivers for the rate of gas nucleation at the surface of gas-evolving electrodes, since they are widely used as key indicators in previous works [47,48]. Our numerical simulations revealed that the dissolved oxygen concentration was significantly influenced by the operating temperature (Fig. 5a–c), where higher temperatures led to lower dissolved oxygen concentrations in the PTL (Fig. 5a–c). This numerical result served as the basis for assuming that dissolved oxygen concentrations were a decreasing function of temperature in the *in operando* imaging work. We thereby attribute the experimentally observed lower oxygen gas saturation to the lower gas evolution rate that would accompany the lower dissolved oxygen concentrations predicted from our numerical simulation. We calculated the change in the dissolved oxygen concentration in water with increasing temperature in the region of interest defined in Fig. 4(a), and observed that the concentration was consistently lower by 50 % when increasing T = 40 °C to T = 80 °C for all tested current densities (Fig. 5d) even though the oxygen solubility decreased by 25 % between these two temperatures [61]. The impact of reducing the dissolved oxygen concentration was far more significant than reducing the oxygen solubility on the gas saturation.

The lower dissolved oxygen concentrations seen in the numerical simulation were attributed to: 1) the improved oxygen diffusivity in liquid water (bulk diffusivity increases from 5.1×10^{-8} m^2/s to 9.9×10^{-8} m^2/s from 40 °C to 80 °C [63]) and 2) the lower gas saturation in the PTL leading to a higher effective oxygen diffusivity in liquid water. We also observed a more uniform dissolved oxygen concentration throughout the PTL at higher temperatures in the numerical simulation (Fig. 4c). We expect this trend in dissolved oxygen concentration uniformity to hold in our experiments, leading to a more uniform gas evolution rate in the experiments. Hence, we attribute the relatively uniform gas saturation observed through neutron imaging to the more uniform dissolved oxygen concentrations predicted from our numerical simulations.

It is important to note that the model presented in this work is 2D and single-phase, which cannot be used to fully characterize the complex two-phase flow behavior in the PTL. A full characterization of the temperature-dependent two-phase flow behavior in a PTL must involve

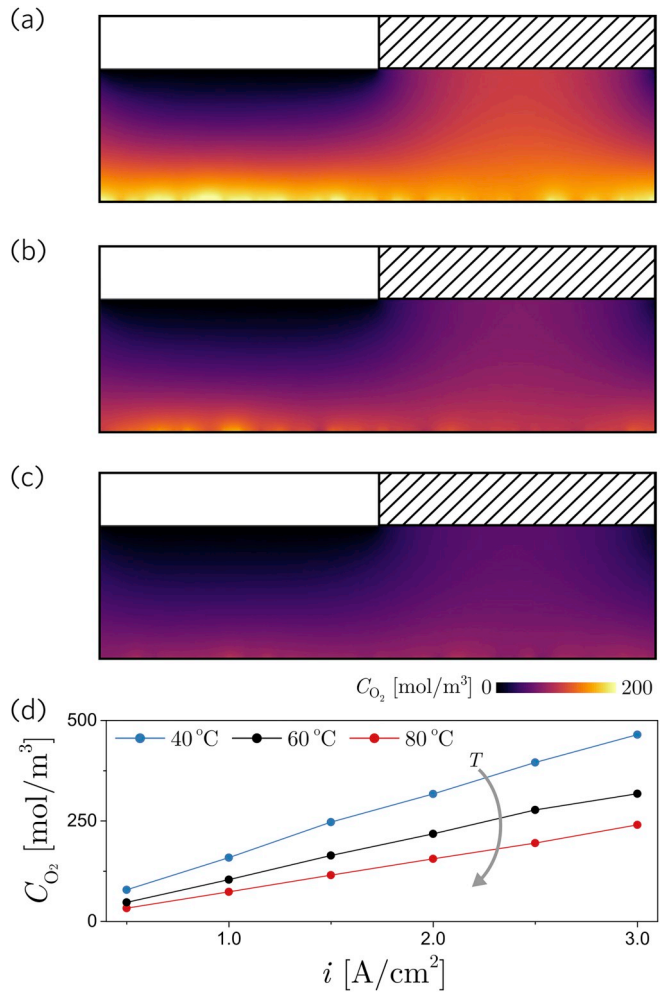

Fig. 5. CFD solutions for the convection-diffusion equation to predict the concentration of dissolved oxygen in liquid water within the PTL. (a-c) The resulting dissolved oxygen concentration contour plots for (a) T = 40 °C, (b) 60 °C, (c) 80 °C at $i = 1.0$ A/cm^2. (d) The average dissolved oxygen concentrations near the CL-PTL interface. Lower dissolved oxygen concentrations were observed at higher operating temperatures.

the simulation of bubble nucleation (i.e. classical nucleation theory or density functional theory [48]), bubble growth (i.e. volume-of-fluid method [64]), and bubble detachment (i.e. balancing the electrostatic force, Marangoni force, and hydrodynamic forces acting on the bubble [65]) and their interactions. Ojong et al. [35] presented an excellent pioneering work in developing a performance model that captures the temperature-dependent two-phase flow behavior in the PTL. The neutron images presented in this work provide first-of-its-kind data that contributes to the characterization of temperature-dependent two-phase flow behavior in the PTL.

3.3. Temperature-dependent mass transport overpotential

We present the electrochemical performance characteristics that were obtained concurrently with neutron imaging. The cell performance improved with higher operating temperatures (Fig. 6a), which is in agreement with previous works [7,8]. We also observed lower mass transport overpotentials at higher operating temperatures (Fig. 6b). We attributed the lower mass transport overpotential at higher operating temperatures to: 1) lower and relatively uniform gas saturation and 2) lower dissolved oxygen concentration near the CL-PTL interface. Lower gas saturation near the CL-PTL interface translates to fewer physical obstructions of liquid water pathways to the reaction sites, which

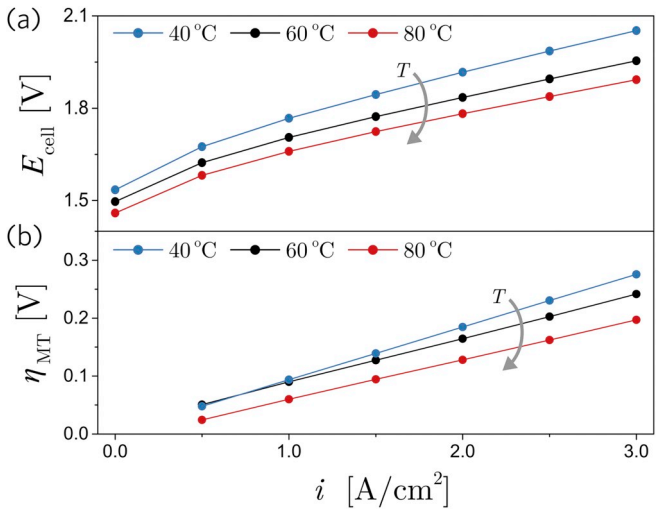

Fig. 6. Electrochemical performance results obtained simultaneously during neutron imaging. (a) Polarization curve for the three operating temperatures. Cell voltage was lower at higher operating temperatures for all current densities. (b) Dependence of mass transport overpotential on temperature. Mass transport overpotential was also lower at higher operating temperatures for all current densities.

subsequently leads to more uniform operating conditions contributing to a lower mass transport overpotential. However, this mechanism alone does not explain the 30 % decrease in mass transport overpotential, since gas saturation decreased by 3 %–15 % from T = 40 °C to T = 80 °C, depending on the operating current density, whereas the decrease in mass transport overpotential is consistent throughout the examined operating current densities.

We compared the trends in mass transport overpotential with the simulated dissolved oxygen concentrations near the CL-PTL interface (Fig. 5d), and observed that both the mass transport overpotential and dissolved oxygen concentration become lower at higher temperatures. Trinke et al. [66] reported that the mass transport overpotential is greatly influenced by the dissolved oxygen concentration in the CL, evidenced by the Nernst overpotential equation:

$$\eta_{nernst} = \frac{RT}{nF} \ln\left(\frac{C_{H_2} C_{O_2}^{\frac{1}{2}}}{C_{H_2O}}\right) \tag{24}$$

where R is the universal gas constant [8.314 J/mol/K], T is the temperature [K], n is the number of electrons transferred per reaction, F is Faraday's constant [96485 C/mol], and C_{H_2}, C_{O_2}, and C_{H_2O} are concentrations of dissolved hydrogen, dissolved oxygen, and water near the reaction sites, respectively [mol/m^3]. A lower dissolved oxygen concentration at the CL-PTL interface leads to a lower Nernst overpotential required to drive the oxygen evolution reaction.

In this work, we provided the first physical explanation of the benefits of increasing operating temperatures for reducing mass transport overpotential (Fig. 6b). The lower gas saturation near the CL-PTL interface at higher temperatures translates to fewer physical obstructions of the reaction sites, resulting in more uniform operating conditions. Furthermore, the dissolved oxygen concentration was lower at higher operating temperatures in our numerical simulations, which suggests that the dissolved oxygen concentration was also lower in our experiment, leading to a decrease in the Nernst overpotential required to drive the oxygen evolution reaction. Here, we demonstrated that a higher operating temperature was beneficial for enhanced oxygen transport in the PTL, verified for operating conditions where $i \leq 3$ A/cm^2 and $\zeta \gg 1$. We note that the results in

this work were based on sintered-powder PTLs and titanium flow fields featuring parallel flow channels, and further investigation is required to determine the role of component design on the temperature-dependent gas saturation in the PTL. Furthermore, a further investigation at higher temporal resolutions is recommended to determine the effect of the two-phase flow regime in the anode flow channels on the gas saturation in the PTL. For example, previous works [36,67] have shown that slug formation in the anode flow channels may lead to the beneficial enhancement of gas removal from the reaction sites via coalescence. Quantifying two-phase flow behavior in both the PTL and the anode flow channels will facilitate a coupled understanding of temperature-dependent gas saturation in the PTL.

4. Conclusions

In this work, we investigated the effect of operating temperature on the gas distribution in the PTL, and we established the first mechanistic understanding of how higher temperature operation leads to reduced mass transport overpotentials. We employed neutron radiation on an operating electrolyzer to visualize the change in gas saturation in the PTL with increasing temperatures (40 °C, 60 °C, and 80 °C) and current densities (0.5 A/cm^2 to 3.0 A/cm^2). We observed that an increase in current density resulted in an increase in gas saturation, but an increase in the operating temperature resulted in a decrease in gas saturation. The gas saturation decreased by up to 15 % as the temperature increased from T = 40 °C to T = 80 °C, which was surprising since oxygen solubility in liquid water is known to decrease with increasing temperature (by 25 % from T = 40 °C to T = 80 °C). Additionally, we observed a more uniform gas saturation distribution at higher temperatures, evidenced by the nearly identical gas saturations in the land region and the channel region.

We calculated the dissolved oxygen concentration in the PTL via 2D computational fluid dynamics to elucidate the mechanistic cause for lower average gas saturations and more uniform gas distributions near the CL-PTL interface. We determined that the dissolved oxygen concentration was consistently lower by 50 % when increasing T = 40 °C to T = 80 °C for all tested current densities in our numerical model. This numerical result informed our *in operando* imaging work, supporting the hypothesis that dissolved oxygen concentrations were also a function of temperature in the experiment. We proposed that the lower dissolved oxygen concentrations were accompanied by lower gas evolution rates in the PTL, thereby providing a mechanistic explanation for the decrease in gas saturation with increasing temperature. Furthermore, we determined from our numerical simulations that the dissolved oxygen concentration became more uniform with increasing temperatures, and this served as the basis for assuming a more uniform gas evolution rate in the PTL in our experiment. Therefore, we attributed the relatively uniform gas saturation observed in our experiments to the more uniform dissolved oxygen concentrations predicted from our numerical simulations.

Lastly, we reported that the mass transport overpotential was a function of the operating temperature (observed experimentally). Two physicochemical mechanisms of this function were revealed: (1) the lower and more uniform gas saturation near the CL-PTL interface at higher temperatures led to fewer reaction site obstructions, and (2) the lower dissolved oxygen concentration near the CL-PTL interface at higher temperatures led to a decreased Nernst overpotential required to drive the reaction. Based on these results, we recommend PEM electrolyzer manufacturers and users to employ higher operating temperatures for optimal water and oxygen transport in the PTL for enhanced performance.

Acknowledgements

Financial support from the Natural Sciences and Engineering Research Council of Canada (NSERC) and the Canada Research Chairs Program are gratefully acknowledged. Also, the authors gratefully acknowledge the financial support of the International Cooperation and Exchange of the National Natural Science Foundation of China (No. 51620105011). Graduate scholarships to ChungHyuk Lee from the Bert Wasmund Graduate Fellowship in Sustainable Energy Research, Hatch Graduate Fellowship for Sustainable Energy Research, David Sanborn Scott Graduate Fellowship, and the Ontario Graduate Scholarship are gratefully acknowledged. NIST authors acknowledge support from the U.S. Department of Commerce, the NIST Radiation Physics Division, the Director's office of NIST, and the NIST Center for Neutron Research.

Appendices.

Appendix A. Tafel slope measurement

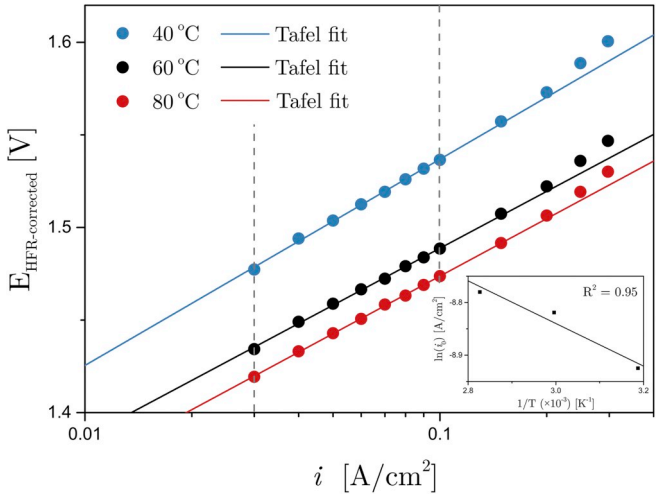

Figure A.1. Tafel plots for determining the kinetic overpotential. The Tafel region was considered from 30 mA/cm2 to 100 mA/cm2, indicated between dashed gray lines. This approximation was justified by the demonstrated Arrhenius relation (inset of figure).

Appendix B. Gas saturation near the porous transport layer and flow field interface

We quantified the average gas saturations in the region near the PTL-FF interface, which we defined as the region bound by the PTL-FF interface and the plane at y = 190 μm (see white-dashed box in Fig. A.2a). We observed the highest overall gas saturation at T = 80 °C throughout the operating current densities, and the lowest overall gas saturation at T = 60 °C (Fig. A.2b). The trend of gas saturation near the PTL-FF interface was unique relative to the trend observed for the gas saturation near the CL-PTL interface (Fig. 4b). These results suggest that the gas transport mechanisms that dominate within these two distinct regions are also distinct from each other. The gas transport behavior near the PTL-FF interface may be affected by factors that are unique to this region, such as the gas detachment frequency within the flow channels or the thermal transport between the land of the flow field and the PTL. On the other hand, the trends in gas saturation near the PTL-FF interface did not exhibit correlations to the trends in mass transport overpotential with increasing temperature (Fig. 6b); therefore, increasing the temperature was found to have a negligible impact on gas saturation near the PTL-FF interface compared to the CL-PTL interface. Further investigations may elucidate other potential temperature-dependent aspects of the electrolyzer that may influence the gas accumulation near the PTL-FF interface, such as the specific cell components used and the operating conditions applied.

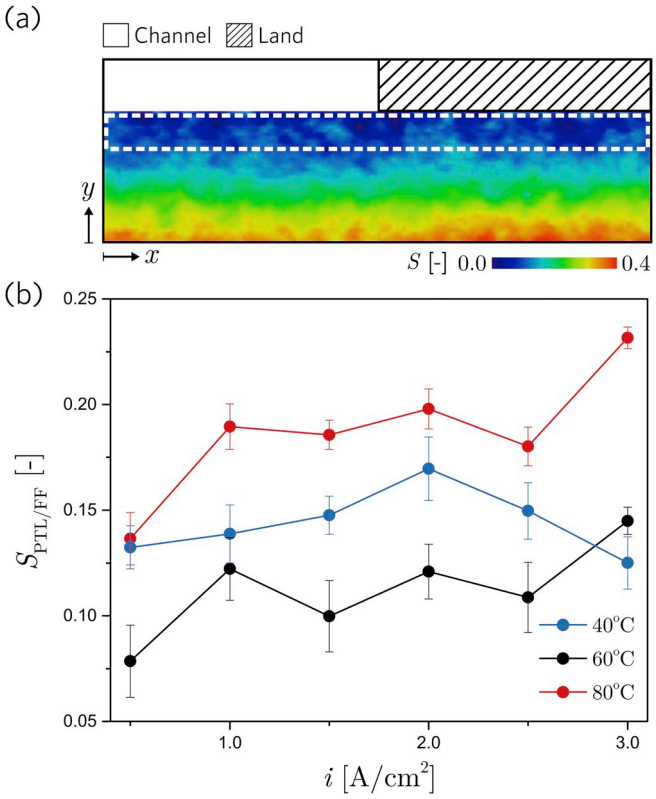

Figure A.2. Oxygen gas distributions near the PTL-FF interface of an operating electrolyzer. (a) We quantified the average gas saturation in the region bounded by $y = 190$ μm and the PTL-FF interface (white-dashed box). (b) Average gas saturations near the PTL-FF interface. We observed the highest gas saturation at 80 °C.

References

[1] A.B. Pittock, Climate Change: Turning up the Heat, Routledge, 2017.
[2] S. Chu, Y. Cui, N. Liu, Nat. Mater. 16 (2017) 16.
[3] J.A. Turner, Science 285 (1999) 687–689.
[4] C.K. Mittelsteadt, ECS Transactions 69 (2015) 205–211.
[5] U. Babic, M. Suermann, F.N. Büchi, L. Gubler, T.J. Schmidt, J. Electrochem. Soc. 164 (2017) F387–F399.
[6] M. Carmo, D.L. Fritz, J. Mergel, D. Stolten, Int. J. Hydrogen Energy 38 (2013) 4901–4934.
[7] Ö.F. Selamet, M.C. Acar, M.D. Mat, Y. Kaplan, Int. J. Energy Res. 37 (2013) 457–467.
[8] M. Suermann, T.J. Schmidt, F.N. Büchi, Electrochim. Acta 211 (2016) 989–997.
[9] J. Kai, R. Saito, K. Terabaru, H. Li, H. Nakajima, K. Ito, J. Electrochem. Soc. 166 (2019) F246–F254.
[10] M. Chandesris, V. Médeau, N. Guillet, S. Chelghoum, D. Thoby, F. Fouda-Onana, Int. J. Hydrogen Energy 40 (2015) 1353–1366.
[11] J.O. Majasan, J.I. Cho, I. Dedigama, D. Tsaoulidis, P. Shearing, D.J. Brett, Int. J. Hydrogen Energy 43 (2018) 15659–15672.
[12] Q. Feng, G. Liu, B. Wei, Z. Zhang, H. Li, H. Wang, J. Power Sources 366 (2017) 33–55.
[13] M. Suermann, T.J. Schmidt, F.N. Büchi, ECS Transactions 69 (2015) 1141–1148.
[14] S. Sun, Y. Xiao, D. Liang, Z. Shao, H. Yu, M. Hou, B. Yi, RSC Adv. 5 (2015) 14506–14513.
[15] P. Millet, A. Ranjbari, F. Guglielmo, S.A. Grigoriev, F. Auprêtre, Int. J. Hydrogen Energy 37 (2012) 17478–17487.
[16] C. Lee, J. Hinebaugh, R. Banerjee, S. Chevalier, R. Abouatallah, R. Wang, A. Bazylak, Int. J. Hydrogen Energy 42 (2017) 2724–2735.
[17] F. Arbabi, A. Kalantarian, R. Abouatallah, R. Wang, J. Wallace, A. Bazylak, J. Power Sources 258 (2014) 142–149.
[18] A. Nouri-Khorasani, E.T. Ojong, T. Smolinka, D.P. Wilkinson, Int. J. Hydrogen Energy 42 (2017) 28665–28680.
[19] P. Lettenmeier, S. Kolb, N. Sata, A. Fallisch, L. Zielke, S. Thiele, A. Gago, K. Friedrich, Energy Environ. Sci. 10 (2017) 2521–2533.
[20] P. Lettenmeier, S. Kolb, F. Burggraf, A.S. Gago, K.A. Friedrich, J. Power Sources 311 (2016) 153–158.
[21] O. Panchenko, E. Borgardt, W. Zwaygardt, F.J. Hackemüller, M. Bram, N. Kardjilov, T. Arlt, I. Manke, M. Müller, D. Stolten, J. Power Sources 390 (2018) 108–115.
[22] O. Panchenko, L. Giesenberg, E. Borgardt, W. Zwaygardt, N. Kardjilov, H. Markötter, T. Arlt, I. Manke, M. Müller, D. Stolten, Energies 12 (2019) 350.
[23] A. Fallisch, L. Schellhase, J. Fresko, M. Zechmeister, M. Zedda, J. Ohlmann, L. Zielke, N. Paust, T. Smolinka, Int. J. Hydrogen Energy 42 (2017) 13544–13553.
[24] J.K. Lee, A. Bazylak, J. Electrochem. Soc. 166 (2019) F1000–F1006.
[25] S.H. Larimi, A. Ramiar, Q. Esmaili, R. Shafaghat, Heat Mass Transf. (2018) 1–8.
[26] J. Garcia-Navarro, M. Schulze, K.A. Friedrich, ACS Sustain. Chem. Eng. 7 (2018) 1600–1610.
[27] K. Bromberger, J. Ghinaiya, T. Lickert, A. Fallisch, T. Smolinka, Int. J. Hydrogen Energy 43 (2018) 2556–2569.

[28] J. Mo, R.R. Dehoff, W.H. Peter, T.J. Toops, J.B. Green, F. Zhang, Int. J. Hydrogen Energy 41 (2016) 3128–3135.
[29] Z. Kang, G. Yang, J. Mo, S. Yu, D.A. Cullen, S.T. Retterer, T.J. Toops, M.P. Brady, G. Bender, B.S. Pivovar, J.B. Green Jr., F. Zhang, Int. J. Hydrogen Energy 43 (2018) 14618–14628.
[30] S. Grigoriev, P. Millet, S. Volobuev, V. Fateev, Int. J. Hydrogen Energy 34 (2009) 4968–4973.
[31] L. Zielke, A. Fallisch, N. Paust, R. Zengerle, S. Thiele, RSC Adv. 4 (2014) 58888–58894.
[32] H. Ito, T. Maeda, A. Nakano, C.M. Hwang, M. Ishida, A. Kato, T. Yoshida, Int. J. Hydrogen Energy 37 (2012) 7418–7428.
[33] V. Fry, J. Selker, S. Gorelick, Water Resour. Res. 33 (1997) 2687–2696.
[34] T.W. de Haas, H. Fadaei, U. Guerrero, D. Sinton, Lab Chip 13 (2013) 3832–3839.
[35] E.T. Ojong, J.T.H. Kwan, A. Nouri-Khorasani, A. Bonakdarpour, D.P. Wilkinson, T. Smolinka, Int. J. Hydrogen Energy 42 (2017) 25831–25847.
[36] Y. Li, Z. Kang, J. Mo, G. Yang, S. Yu, D.A. Talley, B. Han, F. Zhang, Int. J. Hydrogen Energy 43 (2018) 11223–11233.
[37] J. Seweryn, J. Biesdorf, T.J. Schmidt, P. Boillat, J. Electrochem. Soc. 163 (2016) F3009–F3011.
[38] O.F. Selamet, U. Pasaogullari, D. Spernjak, D.S. Hussey, D.L. Jacobson, M. Mat, ECS Transactions 41 (2011) 349–362.
[39] M.A. Hoeh, T. Arlt, N. Kardjilov, I. Manke, J. Banhart, D.L. Fritz, J. Ehlert, D. L. Fritz, W. Lüke, W. Lehnert, ECS Transactions 69 (2015) 1135–1140.
[40] O.F. Selamet, U. Pasaogullari, D.S. Hussey, D.L. Jacobson, M.D. Mat, Int. J. Hydrogen Energy 38 (2013) 5823–5835.
[41] H. Ito, T. Maeda, A. Nakano, Y. Hasegawa, N. Yokoi, C.M. Hwang, M. Ishida, A. Kato, T. Yoshida, Int. J. Hydrogen Energy 35 (2010) 9550–9560.
[42] P. Lettenmeier, R. Wang, R. Abouatallah, B. Saruhan, O. Freitag, P. Gazdzicki, T. Morawietz, R. Hiesgen, A. Gago, K. Friedrich, Sci. Rep. 7 (2017) 44035.
[43] D.S. Hussey, D. Spernjak, A.Z. Weber, R. Mukundan, J. Fairweather, E.L. Brosha, J. Davey, J.S. Spendelow, D.L. Jacobson, R.L. Borup, J. Appl. Phys. 112 (2012).
[44] C. Lee, R. Banerjee, N. Ge, J.K. Lee, B. Zhao, E. Baltic, J.M. LaManna, D.S. Hussey, D.L. Jacobson, R. Abouatallah, R. Wang, A. Bazylak, Electrochim. Acta 279 (2018) 91–98.
[45] D.S. Hussey, D.L. Jacobson, E. Baltic, Nucl. Instrum. Methods Phys. Res. Sect. A Accel. Spectrom. Detect. Assoc. Equip. 651 (2011) 73–76.
[46] A.S. Gago, S.A. Ansar, B. Saruhan, U. Schulz, P. Lettenmeier, N.A. Cañas, P. Gazdzicki, T. Morawietz, R. Hiesgen, J. Arnold, K.A. Friedrich, J. Power Sources 307 (2016) 815–825.
[47] T. Kadyk, D. Bruce, M. Eikerling, Sci. Rep. 6 (2016) 38780.
[48] A. Taqieddin, M.R. Allshouse, A.N. Alshawabkeh, J. Electrochem. Soc. 165 (2018) E694–E711.
[49] Q. Chen, L. Luo, H. Faraji, S.W. Feldberg, H.S. White, J. Phys. Chem. Lett. 5 (2014) 3539–3544.
[50] R. Vetter, J.O. Schumacher, Comput. Phys. Commun. 234 (2019) 223–234.
[51] T. Rosén, J. Eller, J. Kang, N.I. Prasianakis, J. Mantzaras, F.N. Büchi, J. Electrochem. Soc. 159 (2012) F536–F544.
[52] F. Marangio, M. Santarelli, M. Cali, Int. J. Hydrogen Energy 34 (2009) 1143–1158.
[53] J. Gostick, M. Aghighi, J. Hinebaugh, T. Tranter, M.A. Hoeh, H. Day, B. Spellacy, M.H. Sharqawy, A. Bazylak, A. Burns, Comput. Sci. Eng. 18 (2016) 60–74.
[54] S. Chevalier, J. Hinebaugh, A. Bazylak, J. Electrochem. Soc. 166 (2019) F3246–F3254.
[55] A.K.C. Wong, R. Banerjee, A. Bazylak, J. Electrochem. Soc. 166 (2019) F3009–F3019.
[56] R.L. LeRoy, C.T. Bowen, D.J. LeRoy, J. Electrochem. Soc. 127 (1980) 1954–1962.
[57] H. Ito, T. Maeda, A. Nakano, A. Kato, T. Yoshida, Electrochim. Acta 100 (2013) 242–248.
[58] R. Lenormand, E. Touboul, C. Zarcone, J. Fluid Mech. 189 (1988) 165–187.
[59] E.W. Lemmon, M.O. McLinden, D.G. Friend (Eds.), Thermophysical Properties of Fluid Systems, National Institute of Standards and Technology, Gaithersburg MD, 1998.
[60] N. Vargaftik, B. Volkov, L. Voljak, J. Phys. Chem. Ref. Data 12 (1983) 817–820.
[61] D. Tromans, Hydrometallurgy 48 (1998) 327–342.
[62] O.F. Selamet, P. Deevanhxay, S. Tsushima, S. Hirai, J. Power Sources 296 (2015) 133–141.
[63] C. Wilke, P. Chang, AIChE J. 1 (1955) 264–270.
[64] F. Arbabi, H. Montazeri, R. Abouatallah, R. Wang, A. Bazylak, J. Electrochem. Soc. 163 (2016) F3062–F3069.
[65] S. Lubetkin, Chem. Soc. Rev. 24 (1995) 243–250.
[66] P. Trinke, G. Keeley, M. Carmo, B. Bensmann, R. Hanke-Rauschenbach, J. Electrochem. Soc. 166 (2019) F465–F471.
[67] I. Dedigama, P. Angeli, K. Ayers, J.B. Robinson, P.R. Shearing, D. Tsaoulidis, D. J. Brett, Int. J. Hydrogen Energy 39 (2014) 4468–4482.